

Dear Valentina and reviewers,

We would like to thank the reviewers for their valuable input to improving our manuscript.

The point by point responses to the reviewer comments were made in the individual replies we posted as supplements in the discussion (<https://www.the-cryosphere-discuss.net/tc-2018-83/>). Accordingly, rather than repeating those here we simply attach the revised manuscript including all changes highlighted.

We would like to additionally point out three changes that have been made further to those requested in the reviews.

1) While doing the additional sensitivity tests on the slope stability model suggested by reviewer 1, we noticed a coding error causing areal percentage slope stability/instability excluding ponds and ice cliffs to be wrong. We have adjusted the values accordingly in the manuscript and figures. This does not affect the conclusions of the paper, but rather strengthens our argument that relatively large areas of the debris surface are unstable, on the basis that the values that exclude ponds and ice cliffs are now more similar to those that include ponds and ice cliffs.

This led to a change in the text as follows: "Slope stability modelling suggests that, under mid-August ablation conditions, the percentage of the debris-covered area interpreted as potentially unstable for the three study areas of Ngozumpa Glacier is between 13 and 34% including ponds and ice cliffs, and between 12 and 22% 10 and 32% if ponds and ice cliffs are excluded (Fig. 9)."

2) We also noticed that we had used the incorrect colour map in Figure 9d and this has also been corrected in the revised manuscript.

3) The reference to Del Gobbo (2017) was previously missing from the reference list, but has been added now.

1 Supraglacial debris thickness variability: Impact on ablation and relation to
2 terrain properties.

3

4 Lindsey I. Nicholson¹, Michael McCarthy^{2,3}, Hamish Pritchard² and Ian Willis³

5 ¹ *Department of Atmospheric and Cryospheric Sciences, Universität Innsbruck, Innsbruck, Austria.*

6 ² *British Antarctic Survey, United Kingdom Research and Innovation, Madingley Road, Cambridge,*
7 *UK*

8 ³ *Scott Polar Research Institute, University of Cambridge, Cambridge, UK*

9 *Correspondence: lindsey.nicholson@uibk.ac.at*

10

11 **ABSTRACT:** *Shallow ground penetrating radar (GPR) surveys are used to characterize the small-*
12 *scale spatial variability of supraglacial debris thickness on a Himalayan glacier. Debris thickness*
13 *varies widely over short spatial scales. Comparison across sites and glaciers suggests that the*
14 *skewness and kurtosis of the debris thickness frequency distribution decrease with increasing*
15 *mean debris thickness, ~~and we.~~ We hypothesise that this is related to the degree of gravitational*
16 *reworking the debris cover has undergone, and the effects of progressive stagnation of the*
17 *underlying ice and is therefore a proxy for the maturity of surface debris covers. In the cases tested*
18 *here, using a single mean debris thickness value instead of accounting for the observed small-scale*
19 *debris thickness variability underestimates modelled midsummer sub-debris ablation rates by 11-*
20 *30 %. While no simple relationship is found between ~~measured-local~~ debris thickness and*
21 *morphometric terrain parameters, analysis of the GPR data in conjunction with high-resolution*
22 *terrain models provides some insight to the processes of debris gravitational reworking. Periodic*
23 *sliding failure of the debris, rather than progressive mass diffusion, appears to be the main process*
24 *redistributing supraglacial debris. ~~The incidence of sliding is controlled by slope, aspect, upstream~~*
25 *~~catchment area and debris thickness via their impacts on predisposition to slope failure and~~*
26 *~~meltwater availability at the debris-ice interface.~~ Slope stability modelling for samples of glacier*
27 *terrain suggests that the percentage of the debris-covered glacier surface area subject to debris*
28 *instability can be considerable at glacier scale, indicating that up to 22.% of the debris covered*
29 *area is susceptible to developing ablation hotspots associated with patches of thinner debris.*

30 1. Introduction

31 Debris-covered glaciers are the dominant form of glaciation in the Himalaya (e.g. Kraaijenbrink
32 et al. 2017), and are common in other tectonically active mountain ranges worldwide (Benn et
33 al. 2003). Supraglacial debris cover alters the rate at which underlying ice melts in comparison
34 to clean ice in a manner primarily governed by the thickness of the debris cover (e.g. Østrem,
35 1959; Loomis, 1970; Mattson et al., 1992; Kayastha et al. 2000; Nicholson and Benn, 2006; Reid
36 and Brock, 2010): A thin supraglacial debris cover (< a few cm) enhances melt, while thicker
37 debris cover reduces melt by insulating the ice beneath from surface energy receipts. Prevailing
38 weather conditions, and local debris properties, such as albedo, lithology, texture and moisture
39 content, also influence the amount of energy available for sub-debris ablation, and modify the
40 exact relationship between debris thickness and ablation rate, ~~–. However, but~~ the general
41 characteristics of the so-called Østrem curve are robust, ~~further~~ demonstrating the dominant
42 role of debris thickness in this relationship (Fig. 1).

43 Both theory and observations indicate that the spatial variability of supraglacial debris
44 thickness typically has both a systematic and a non-systematic component. Debris thickness
45 tends to increase towards the glacier margins and terminus due to concentration by
46 decelerating ice velocity, and increasing background meltout rate (e.g. Kirkbride, 2000). This
47 systematic variation is evident in field measurements of debris cover thickness (e.g. Zhang et al.,
48 2011), and in characterizations of debris thickness as a function of the surface temperature
49 distribution observed from satellite imagery (e.g. Mihalcea et al. 2006; Mihalcea et al. 2008a;
50 Mihalcea et al. 2008b; Foster et al. 2012; Rounce and McKinney, 2014; Schauwecker et al. 2015;
51 Gibson et al. 2017). At local scales, debris thickness varies less systematically according to the
52 input distribution, local meltout patterns and gravitational and meltwater reworking of the
53 supraglacial debris. Manual excavations (e.g. Reid et al., 2012), observations of debris thickness
54 made above exposed ice cliffs (e.g. Nicholson and Benn, 2012; Nicholson and Mertes 2017), and
55 debris thickness surveyed by ground penetrating radar (McCarthy et al., 2017) demonstrate
56 that debris thickness varies considerably over short horizontal distances. Thus, the thickness of
57 debris over a sampled area of glacier surface is better expressed as a probability density
58 function than a single value (e.g. Nicholson and Benn, 2012; Reid et al., 2012). This is important
59 because, given the strongly non-linear relationship between ablation rate and debris thickness
60 (Fig. 1), patches of thinner debris within a generally thicker supraglacial debris cover can be
61 expected to contribute disproportionately to glacier ablation in a manner analogous to exposed
62 ice faces ~~Exposed ice faces within debris-covered glacier ablation areas are known to contribute~~
63 ~~disproportionately to glacier ablation compared to their area (e.g. Sakai et al., 2000; Juen et al.,~~
64 ~~2014; Buri et al., 2016; Thompson et al., 2016). Indeed, and it has been proposed that such~~
65 ~~'ablation hotspots', along with stagnation, are the reasons for the observed similarity in surface~~
66 ~~lowering rates of otherwise comparable clean and debris-covered ice surfaces (e.g. Käab et al.,~~
67 ~~2012, Nuimura et al., 2012).~~

68 The limited available data shows the probability density functions or frequency distribution of
69 debris thickness at a glacier or local scale to show varying degrees of kurtosis and typically a
70 positive skew (e.g. Reid et al., 2012; Nicholson and Benn 2012), but the degree to which the
71 frequency distribution deviates from normal, and the controls on the degree of kurtosis and
72 skewness have not been well investigated. Nevertheless, some postulations can be made based

73 upon the systematic and non-systematic variability components described above. As thick
74 debris cover tends to form where there is little to no ice flux it follows that glaciers close to
75 steady state will tend to be dominated by thin debris, causing the debris thickness frequency
76 distribution to have a positive skew, while this might be expected to be less pronounced in
77 sluggish debris-covered glacier termini, or even have a negatively skewed distribution on
78 stagnant glacier tongues or rock glaciers, where ice flux is minimal. Glaciers with patchy debris
79 at the surface are also more likely to have a positively skewed debris thickness distribution than
80 continuously covered glacier surfaces due to gradual topographic inversion and lateral dispersal
81 of debris from localised surface deposits (Anderson, 2000; Kirkbride and Deline 2013). Gently
82 sloping smooth surfaced debris covered glaciers might be expected to experience less
83 gravitational sliding than steeper or more chaotic glacier surfaces, and less gravitational
84 reworking may favour relatively higher kurtosis than at sites where sliding and slope failures
85 are common, and the frequency distribution of debris thickness can be rapidly reworked and
86 potentially even develop multimodal distributions with many areas of thin, recently destabilized
87 debris and also many areas of thick debris where material from slope failures has accumulated.

88

89 ~~Exposed ice faces within debris covered glacier ablation areas are known to contribute~~
90 ~~disproportionately to glacier ablation compared to their area (e.g. Sakai et al., 2000; Juen et al.,~~
91 ~~2014; Buri et al., 2016; Thompson et al., 2016), and it has been proposed that such ‘ablation~~
92 ~~hotspots’, along with stagnation, are the reasons for the observed similarity in surface lowering~~
93 ~~rates of otherwise comparable clean and debris covered ice surfaces (e.g. Käab et al., 2012,~~
94 ~~Nuimura et al., 2012). Given the strongly non-linear relationship between ablation rate and~~
95 ~~debris thickness (Fig. 1), patches of thinner debris within a generally thicker supraglacial debris~~
96 ~~cover can similarly be expected to contribute disproportionately to glacier ablation. Sub-debris~~
97 ~~ice ablation calculations are commonly performed using the mean debris thickness over a~~
98 ~~portion of the glacier surface derived, for example, from satellite thermal imagery (e.g. Fyffe et~~
99 ~~al., 2014) yet given a skewed local debris distribution, in conjunction with the asymptotic~~
100 ~~decline in ablation rate with increasing debris thickness (Fig. 1), calculations of sub-debris ice~~
101 ~~ablation rate and meltwater production using spatially-averaged mean debris thickness may~~
102 ~~differ substantially from the actual meltwater generated from a debris layer of highly variable~~
103 ~~thickness within the same area. Reid and others (2012) offered a first consideration of this~~
104 ~~effect when they applied a distributed glacier ablation model by assigning debris thicknesses to~~
105 ~~debris covered glacier pixels by random sampling of a probability distribution based on a set of~~
106 ~~high resolution field measurements. However, as yet no modelling study has explored in detail~~
107 ~~the interplay between the local debris thickness variability and the local Østrem curve, in terms~~
108 ~~of its net effect on calculated sub-debris ablation., but this has only rarely been considered~~
109 ~~(Reid et al., 2012). The implication of this would be that calculations of sub-debris ice ablation~~
110 ~~rate and meltwater production using spatially-averaged mean debris thickness may differ~~
111 ~~substantially from the actual meltwater generated from a debris layer of highly variable~~
112 ~~thickness within the same area. Therefore, there remains a critical need to be able to quantify~~
113 ~~not only mean supraglacial debris thickness, but also local debris thickness variability, in order~~
114 ~~to understand how debris cover is likely to impact glacier behaviour, meltwater production and~~
115 ~~contribution to local hydrological resources and global sea level rise. Therefore,~~

116 ~~Given the paucity of data on local debris thickness variability there remains a~~
117 ~~critical need to be able to quantify not only mean supraglacial debris thickness, but also local~~
118 ~~debris thickness variability, and assess its impact on ablation rate in order to understand how~~
119 ~~debris cover is likely to impact glacier behaviour, meltwater production and contribution to~~
120 ~~local hydrological resources and global sea level rise.~~

121 ~~Given the potentially significant role of accounting for debris thickness variability on glacier-~~
122 ~~wide ablation rates, it would be advantageous to be able to characterize local debris thickness~~
123 ~~variability. Meeting this need requires a better understanding of debris thickness variability and~~
124 ~~the controls upon it, ideally~~ by means of more readily observable properties. Topographic data
125 has been used to predict soil thickness on hilly, extraglacial terrain under the assumption of
126 steady state conditions (e.g. Pelletier and Rasmussen, 2009). However, associated soil thickness
127 relationships as a function of slope curvature (Heimsmath et al., 2017) are based on progressive
128 creep processes, while reworking of supraglacial debris cover occurs mainly as a result of
129 gravitational instabilities such as ‘topples, slides and flows’ (Moore, 2017). Nevertheless, as the
130 debris thickness that can be supported on a slope is related to slope angle, debris texture and
131 saturation conditions (Moore, 2017) it might still be possible to find explicit relationships
132 between topography and debris thickness. If high-resolution topography data, which is
133 increasingly widely available, could be used to indicate local debris thickness variability, such
134 information would complement spatially averaged mean supraglacial debris thickness values
135 derived by other methods (cf. Arthern et al. 2006).

136 137 **2. Aim of the study**

138 This study investigates ~~the evidence for~~ small-scale debris thickness variability, assesses the
139 impact of local debris thickness variability on calculated sub-debris ice ablation rates, and
140 explores the potential for predicting local debris thickness variability from morphometric
141 terrain parameters. First, debris thickness data from shallow ground penetrating radar surveys
142 are used to characterize the small-scale spatial variability of debris thickness on a Himalayan
143 glacier, examine evidence of gravitational reworking processes and compare the observed
144 variability to previously published data. Second, the impact of the observed small-scale debris
145 thickness variability on modelled sub-debris ablation rates is assessed. Third, a
146 contemporaneous high resolution terrain model and optical imagery are employed to determine
147 if the observed thickness variability can be ~~predicted from related to~~ more readily measured
148 surface terrain properties. Finally, a slope stability model is calibrated with the GPR and
149 ablation model data and used to determine the percentage ~~area~~ of our study ~~areas-sites~~ in the
150 debris-covered ablation zone that are subject to debris instability, and potentially the formation
151 of ablation hotspots, in mid-ablation season (August) conditions.

152 153 **3. Study site and data**

154 The Ngozumpa glacier is a large dendritic debris-covered glacier of the Eastern Himalaya,
155 located in the upper Dudh Kosi catchment, Khumbu Himal, Nepal (Fig. 2a). The glacier has a
156 total area of 61 km² of which the lower 22 km² is heavily debris-covered, with hummocky
157 surface relief in the order of 50m over distances of 100m (Fig. 2b), studded with supraglacial

158 ponds and exposed ice cliffs (Benn et al., 2001). The NE and E branches are no longer connected
159 dynamically to the main trunk (Thompson et al., 2016), which is fed solely by the W branch
160 descending from the flanks of Cho Oyu (8188 m). The southernmost 6.5 km of the glacier is
161 nearly stagnant (Quincey et al. 2009) and has a low surface slope of $\sim 4^\circ$. The terrain of this
162 glacier, its wasting processes and the evolution of surface lakes have been well studied through
163 a series of previous publications (Benn et al., 2000 ~~&-and~~ 2001; Thompson et al., 2012 ~~&-and~~
164 2016), as have the debris properties including limited measurements of debris thickness
165 (Nicholson and Benn, 2012).

166 Debris thickness over much of the debris-covered area is in excess of 1.0 m precluding
167 widespread manual excavation. However, in 2001 measurements of debris thicknesses exposed
168 above ice cliffs were made by theodolite survey at ~ 1 and 7 km from the terminus (Nicholson
169 and Benn, 2012). These data provided only coarse estimates of debris thickness as neither the
170 slope angle of the debris exposure, nor the impact of the theodolite bearing angle were
171 accounted for in the vertical offsetting used to obtain the debris thickness. In April 2016
172 terrestrial photogrammetry was used to create a high resolution scaled model of the local
173 glacier surface from which debris thickness estimates were made in a manner analogous to the
174 theodolite survey at a location ~ 2 km from the terminus near Gokyo village (Nicholson and
175 Mertes, 2017). At the same time, several GPR surveys, totalling 3301 m, were undertaken in this
176 area and a single 238 m GPR survey was done close to the glacier margin ~ 1 km from the glacier
177 terminus (Fig. 2a). Meteorological data are not available from the Ngozumpa glacier surface at
178 this site, so the ablation model was forced using ~~several years of~~ meteorological data measured
179 at the Pyramid weather station (27.95° N / 86.81° E, 5035 m a.s.l.) operated by the Ev-K2-CNR
180 consortium (<http://www.evk2cnr.org/cms/en>) in the neighbouring valley. A digital terrain
181 model generated from Pleiades tri-stereo imagery acquired in April 2016 (Rieg et al., 2018) is
182 used to relate the measured debris thicknesses to the glacier surface terrain.

183

184 **4. Methods**

185

186 4.1 GPR debris thickness data collection and processing

187 GPR measurements were made between 31st March and 20th April 2016 broadly following the
188 methods of McCarthy et al. (2017). Debris thickness was sampled in 36 individual radar
189 transects, covering sloping and level terrain with coarse and fine surface material. The GPR
190 system was a dual frequency 200/600MHz IDS RIS One, mounted on a small plastic sled and
191 drawn along the surface. Data were collected to a Lenovo Thinkpad using the IDS K2 FastWave
192 software. This system produces two simultaneous radargrams for each acquisition. The 200
193 and 600 MHz antennas have separation distances of 0.230 m and 0.096 m respectively. Data
194 acquisition used a continuous step size, a time window of 100 ms and a digitization interval of
195 0.024 ns. The location of the GPR system was recorded simultaneously at 1 s intervals by a low
196 precision GPS integrated with the IDS which assigns a GPS location and time directly to every
197 twelfth GPR trace, and by a more accurate differential GPS (dGPS) system consisting of a
198 Trimble XH and Tornado antenna mounted on the GPR and a local base station of a Trimble
199 Geo7X and Zephyr antenna.

200 Radargrams were processed in REFLEXW (Sandmeier software) by applying the steps shown in
201 Table 1. The reflection at the ice surface was picked manually wherever it was clearly
202 identifiable and was not picked if it was indistinct. The appropriate signal velocity for the
203 supraglacial debris was obtained by burying a 1.5 m long steel bar to a known depth and then
204 passing the GPR over the buried target and picking the two-way travel time to its reflection (Fig.
205 3-a and b). Both fine and coarse material gave similar wave speeds (0.15 and 0.16 m ns⁻¹). These
206 were averaged to obtain a bulk value that is considered representative for all the radar lines
207 measured and is comparable to values from the debris-covered Lirung glacier, central Nepal
208 (McCarthy et al., 2017). Debris thickness was calculated using ice surface two-way travel times
209 and the mean of the two wave speed measurements (0.16 m ns⁻¹), taking the geometry of the
210 GPR system into account. Uncertainties were propagated according to McCarthy et al (2017)
211 and range from 0.14-0.83 m, generally increasing with debris thickness. According to McCarthy
212 et al (2017), transmitter blanking is limited to one wavelength below the surface and so
213 minimum detectable debris thickness is roughly equal to the ratio of debris wave speed to radar
214 frequency. In our case this would imply minimum detectable debris thickness of 0.27 m with the
215 600 MHz antenna and 0.80 m with the 200 MHz antenna.

216 During processing, the integrated GPS locations (typical accuracy of ~ 3 m) were substituted for
217 dGPS locations (typical post-processed accuracy of < 0.05 m) by matching GPS and dGPS
218 timestamps. Where differential correction was not possible due to a lack of visible satellites, the
219 integrated GPS locations were used. The locations of GPR data collected between timestamps
220 were interpolated linearly in REFLEXW. Where the ice surface was identifiable in radargrams of
221 both frequencies, the measurement made using the higher frequency was assigned because
222 higher frequencies give higher precision. GPR data quality was assessed by comparing debris
223 thicknesses calculated using picks from the two different frequencies in the same location (Fig.
224 3c) and by comparing debris thicknesses at transect crossover points (Fig. 3d). In both cases,
225 points fit well to the 1:1 line. To show how debris thickness varies with topography, radargrams
226 were topographically corrected for display purposes after the ice interface had been picked.
227 Debris thickness data was extracted from the picked ice surface at approximately 0.02 m ground
228 spacing for subsequent data analysis.

229 4.2 Ablation modelling

230 In the absence of suitable field measurements of sub-debris ice ablation, a model of ice ablation
231 beneath a debris cover was applied to assess the impact of debris thickness variability on
232 calculated ablation rates. As recent, high quality, local meteorological data are not available to
233 force a time-evolving numerical model, typical ablation season conditions measured at the
234 nearby Pyramid weather station were used to force a steady-state model of sub-debris ice
235 ablation that has been previously published and evaluated against field data (Evatt et al., 2015).

236 Ice ablation conditions are generally restricted to the summer months in the eastern Nepalese
237 Himalaya (Wagnon et al., 2013). For the illustrative simulations performed here, the model was
238 forced with mean August meteorological conditions from 2003-2009 (<2% of August hourly
239 data are missing), and assuming the ice temperature to be 0°C. This provides forcing variables
240 of air temperature (3.27°C), incoming shortwave (208 Wm⁻²) and longwave (314 Wm⁻²)
241 radiation, wind speed (1.94 ms⁻¹) and relative humidity (97%). Appropriate debris properties

242 for dry debris in summer time on the Ngozumpa glacier were adopted from Nicholson and Benn
243 (2012), whereby debris properties of effective thermal conductivity, dry surface albedo and
244 porosity were taken to be $1.29 \text{ Wm}^{-1} \text{ K}^{-1}$, 0.2 and 0.3 respectively. Ice albedo, debris thermal
245 emissivity and the debris surface roughness length, friction velocity and exponential decay rate
246 of wind were adopted from Evatt et al. (2015).

247 The model is used to generate an \dot{Q} strem curve and associated surface debris temperature for
248 the stated inputs, as a function of debris thickness. The model does not account for variability in
249 surface energy receipts due to local ~~topoclimate or surrounding terrain~~, or the effects of spatially
250 or temporally variable debris properties other than thickness, and the chosen input properties
251 are only approximate. However, this does not preclude its illustrative use in investigating the
252 influence of variable debris thickness on calculated ablation rate. ~~Ablation m~~Modelling was
253 carried out ~~using the same forcing data for three sites for which varying only the~~-local debris
254 thickness ~~information data is available~~determined at: (i) the ~~M~~margin study ~~area-site~~ ~1km
255 from the glacier terminus, (ii) the main Gokyo study ~~area-site~~ ~2 km from the terminus, both
256 measured by GPR in 2016, and (iii) the ~~U~~upglacier study ~~area-site~~ ~7 km from the terminus,
257 measured by theodolite survey in 2001 (Fig. 2). Ablation rate and surface temperature ~~is~~
258 calculated for the mean debris thickness is compared to that yielded by multiplying the
259 percentage frequency distribution of debris thickness with the modelled \dot{Q} strem and surface
260 temperature curves. Ablation totals for the month of August are calculated and that derived
261 using the mean debris thickness value is expressed as a percentage deviation of that derived
262 using locally variable debris thickness. Used in this form we assume the model itself to be error
263 free. To isolate the error associated with debris thickness, all other model inputs are also
264 assumed to be error free. Each GPR debris thickness has an associated error, but as no
265 quantified error assessment is available for the thickness values measured by theodolite at 7 km
266 from the terminus a fixed error of $\pm 0.15 \text{ m}$ was applied to these data. The model was run with
267 maximum and minimum debris thickness values according to the assigned errors, to provide an
268 indication of uncertainty of the reported percentage difference in monthly total ablation.

269 4.3 Terrain analysis

270 In order to assess the static relationship between the debris distribution and terrain properties,
271 we used a 5 m resolution digital terrain model (DTM) derived from Pléiades optical tri-stereo
272 imagery taken during the field campaign on the 12th April 2016. The DTM was generated from
273 photogrammetric point clouds extracted from the Pléiades imagery, using a semi-global
274 matching (SGM) algorithm (Hirschmüller, 2008) within the IMAGINE photogrammetry suite of
275 ERDAS IMAGINE. The three images of each triplet were imported and the rational polynomial
276 coefficients (RPC) provided with the Pléiades data were used to define the initial functions for
277 transforming the sensor geometry to image geometry. With those transformation functions,
278 individual geometries of each image in the triplet were orientated relative to each other. To
279 obtain the most accurate exterior orientation possible, initial RPC functions were refined using
280 automatically-extracted tie points. The calculated point clouds were then filtered for outliers,
281 mainly found in very steep and shaded areas, using local topographic 3D filters applied in SAGA
282 GIS software, and converted into a 5 m-resolution DTM using the average elevation of all points
283 within one raster cell as the elevation value for the cell. Gaps were present in very steep areas,
284 where there was cloud, and in areas with low contrast because of fresh snow or liquid water.

285 Terrain properties were extracted using the ArcGIS tools Slope, Aspect and Curvature. GPR data
286 were resampled to the same resolution as these rasters (5 m) by taking the mean of the
287 measurements that occurred within each pixel. This was done using the Point to Raster tool in
288 ArcGIS. GPR data within 5 m of ice cliffs were excluded for comparisons made between debris
289 thickness and topography, in order that their slope, aspect and curvature were not
290 misrepresented. Similarly, GPR data for which dGPS locations were not available were excluded
291 due to their lack of positional accuracy.

292 Ponded water at the surface is associated with the deposition of layers of fine sediments and
293 rapid sedimentation by marginal slumping (Mertes et al., 2017). The recent history of ponded
294 water on the parts of the glacier surface sampled by the radar transects was mapped using air
295 photographs from 1984 ([see Washburn, 1989 for details](#)), and seven cloud-free optical satellite
296 images spanning 2008-2016. ~~These~~ [The satellite](#) images consisted of six Digital Globe images,
297 [and](#) one CNES/Astrium image, all obtained via Google Earth, and the optical image from the
298 2016 Pleiades acquisition used to generate the DTM.

299 4.4 Slope stability modelling and classification

300 Slope stability modeling was carried out following Moore (2017). For the three study areas
301 shown in Fig. 2, debris was classified as either stable or unstable. Unstable debris was further
302 classified as being unstable due to:

- 303 1. Oversteepening, where surface slope exceeds the debris-ice interface friction coefficient,
- 304 2. Saturation excess, where the modeled water table height is greater than the debris
305 thickness, and
- 306 3. Meltwater weakening, where the modeled water table height is less than the debris
307 thickness, but debris pore pressures are sufficiently raised to cause instability.

308 Surface slope (see Section 4.3), modeled midsummer ablation rate (see Section 4.2), upstream
309 contributing area, and mean debris thickness (see Section 4.1) were used as inputs to the
310 model. Upstream contributing area was determined from the DTM in ArcGIS using the Flow
311 Direction and Flow Accumulation tools. Sinks in the DTM were filled if they were less than 3 m
312 deep, following Miles et al (2017), using the ArcGIS Sink and Fill tools. Surface water flowpaths
313 were also determined using the Stream To Feature tool.

314 The model also requires input values for the debris-ice interface friction coefficient, the
315 densities of water and wet debris, and the saturated hydraulic conductivity of the debris. A
316 value of 0.5 was used for the debris-ice interface friction coefficient, following Barrette and
317 Timco (2008) and Moore (2017). Values of 1000 and 2190 kg m⁻³ were used for the densities of
318 water and wet debris, respectively, where wet debris was assumed to have a porosity of 0.3,
319 after Conway and Rasmussen (2000), and the density of rock was assumed to be 2700 kg m⁻³
320 after Nicholson and Benn (2006). The saturated hydraulic conductivity of the debris, which is
321 the parameter around which there is most uncertainty, was determined using the GPR data.
322 Sections of the GPR transects, and subsequently their corresponding DTM pixels, were defined,
323 by visual inspection on the basis of the debris morphology, as either stable or unstable. Sections
324 of thin debris on steep slopes were considered to be unstable if they occurred among sections of
325 thick debris on [shallow-gentle](#) slopes. Sections of anything not considered to be unstable were

326 considered to be stable. Debris stability was then modeled for the same DTM pixels using a wide
327 range of conductivity values. The conductivity value that minimized the difference between the
328 number of pixels that were modeled and observed as being stable or unstable was considered to
329 be optimal. Minimization was carried out using ROC analysis, following Fawcett (2006) and
330 Herreid and Pellicciotti (2017). The resulting saturated hydraulic conductivity value of 40 m d^{-1}
331 is well within the expected range of 10^{-7} - 10^3 m d^{-1} (Fetter, 1994), and is consistent with the
332 debris being well-drained. In order to assess the robustness of the slope stability model,
333 sensitivity tests were carried out for each study area, in which key variables of the slope
334 stability model (ratio of densities of water to debris; saturated hydraulic conductivity; debris-
335 ice interface friction coefficient; debris thickness and calculated daily melt rate) were
336 perturbed, one at a time, by $\pm 10\%$. The percentage of the study area classified as unstable, as
337 well as percentage change from that study area's areal percentage instability (using the best
338 estimate values given above), was recorded for each perturbation.

339 The percentage areal coverage of debris instability was calculated for each of the three study
340 areas (Fig. 2). This was done both including and excluding ice cliffs and ponds, where ice cliffs
341 and ponds were manually digitized from the orthophoto associated with the DTM.

342 The GPR data, DTM and associated orthophoto were collected in March/April 2016, while slope
343 stability modeling was carried out using midsummer (August) ablation rates. It is likely that the
344 debris on a given slope becomes more or less stable seasonally with changes in ablation rates.
345 However, GPR observations of debris instability in March/April are likely to be representative
346 of midsummer debris instability for saturated hydraulic conductivity as maximum melt is
347 expected in midsummer. Similarly, while pond incidence and area vary seasonally on Himalayan
348 glaciers, recurrence rates seasonal ponds commonly reform at the same sites are generally high
349 (Miles et al., 2016), so manually digitized ponds and ice cliffs for March/April are assumed to be
350 broadly representative of ponds and ice cliffs in midsummer for percentage area debris
351 instability calculations excluding ponds and ice cliffs. Finally, model results should be treated
352 only as a best approximation because the model assumes debris thickness and ablation rate are
353 spatially homogeneous in each study area, which, as discussed by Moore (2017), is clearly not
354 the case.

355 5. Results and discussion

356

357 5.1 GPR debris thickness and variability

358 The quality of the GPR data is generally high. The ice surface was clearly identifiable through the
359 debris in the majority of the radargrams collected. This is likely because the GPR system was
360 used in 'continuous-mode' and appropriate acquisition parameters were used. For those
361 radargrams in which the ice surface was not easily identifiable, the debris was appeared to be
362 generally too thick to detect. This-While this means there is the possibility of a slight thin bias in
363 the data. However, it is reasonable to assume the impact is minimal because penetration depths
364 was often greater than 7 m, which is likely near the maximum debris thickness exceed the
365 thickness of any supraglacial debris exposures observed in the field (Nicholson and Benn, 2012;
366 Nicholson and Mertes, 2017). Debris thickness was found to be highly variable with a total
367 range of 0.18 to 7.34 m (Fig. 4 and examples in Fig. 5). There is coherent structure to the debris

368 thickness variation along transects (Fig. 4): In some areas, changes in debris thickness along the
369 transect are gradual, while in a number of cases, there are abrupt changes in debris thickness
370 along a transect associated with pinning points or topographic hollows and cavities in the
371 underlying ice, which the debris cover fills (see Section 5.3 and Fig. 67).

372 Simple statistics of the debris thickness derived from the GPR samples of this study compared
373 with debris thickness datasets available from other glaciers are given in Table 2. Mean debris
374 thickness measured by GPR towards the glacier margin is thicker, and shows wider spread and
375 lower skewness and kurtosis, than the GPR thickness data collected at the Gokyo study area
376 (Table 2; Fig. 4; Fig. 5a-c). The percentage frequency histogram of GPR debris thickness from the
377 glacier margin has a similar shape, but a positive offset compared to data obtained by surveying
378 of ice faces about 1 km from the glacier terminus in 2001, while the GPR data from Gokyo agrees
379 closely with the estimates of debris thickness from the photographic terrain model (Nicholson
380 and Mertes, 2017). The 2001 surveyed debris thickness data from further upglacier (Nicholson
381 and Benn, 2012) is thinner, more skewed, and has higher kurtosis than the sites further
382 downglacier (Fig. 5a-c). Clearly, while debris thickness shows small-scale variability in all cases
383 on the Ngozumpa glacier, the details of that variability differ from site to site. This pattern of
384 change agrees with the tentative hypotheses proposed in the introduction, whereby the
385 downglacier progression of greater debris cover maturity, increasingly stagnant ice and
386 increasing activity of gravitational reworking on the hummocks terrain studded with ice cliffs
387 and ponds all serve to gradually reduce the skew and kurtosis of the debris thickness
388 distribution.

389 ~~Clearly, while debris thickness shows small-scale variability in all cases on the Ngozumpa~~
390 ~~glacier, the details of that variability differ from site to site. This is also observed when pattern is~~
391 ~~supported by considering~~ data from other glaciers (Table 2; Fig. 5). The medial moraine on Haut
392 Glacier d’Arolla emerged during glacial recession in the second half of the 20th century (Reid et
393 al., 2012), offering an example of a recently developed debris cover. The debris-covered part of
394 Suldenferner developed its continuous debris cover since the beginning of the 19th century,
395 when the glacier was mapped with debris cover below ~2500 m and only surficial medial
396 moraine bands extending up to 2700 m (Finsterwalder and Lagally, 1913). The Nepalese
397 glaciers are thought to have been debris-covered for longer (Rowan, 2016), although it remains
398 unclear when their debris covers first developed.

399 The Lirung glacier measurements appear broadly more similar to sites further downglacier on
400 the Ngozumpa glacier. Debris thickness at the Lirung glacier, central Nepal, which like the lower
401 Ngozumpa glacier supports a thick debris cover overlying stagnant ice shows a bimodal
402 distribution not replicated at the other sites, but partially seen in the Ngozumpa Margin site
403 (Fig. 5a). This is At Lirung, this is suspected to be due at least partly due to sampling bias, as the
404 measurements were made to test the GPR method rather than to characterize typical debris
405 thickness at this glacier. However, the hummocky terrain of Lirung glacier (cf. Fig. 2b), dissected
406 with ponds and ice faces, is likely to facilitate widespread debris slope failure, which would
407 more readily cause multimodal distributions of debris thickness. In contrast, debris thickness
408 variability at the Alpine sites shown here is more comparable to that of the upper Ngozumpa.
409 The less mature debris cover on Suldenferner, in the Italian Alps, is generally thinner and the
410 terrain is less hummocky, with relief primarily associated with incision by supraglacial streams

411 ~~At Suldenerferner, in the Italian Alps, debris~~Debris thickness measured across the whole debris-
412 covered area by excavation, and along cross- and down-glacier transects by GPR, shows a
413 substantially thinner mean than the Himalayan cases, with greater ~~skewness and~~ kurtosis. The
414 GPR lines sampled at Suldenerferner crossed thick medial moraines and this sampling bias may
415 explain the distribution being less skewed than that determined from the excavations covering
416 the whole debris covered area. This highlights a further problem in sampling strategy for
417 meaningful determinations of debris thickness variability at a local and glacier scale, as the
418 locally less skewed distributions are presumably applicable only to sections of the glacier
419 surface containing these medial moraines, while the debris covered ablation area as a whole
420 shows a more skewed distribution of debris thickness. The debris cover on the medial moraine
421 of Haut Glacier d'Arolla in the Swiss Alps is even thinner with yet more pronounced skewness
422 and kurtosis. ~~Thus, debris thickness variability at the Alpine sites shown here is more~~
423 ~~comparable to that of the upper Ngozumpa, while the Lirung glacier measurements appear~~
424 ~~broadly more similar to sites further downglacier on the Ngozumpa glacier. This is inkeeping~~
425 ~~with its younger age and what might be expected from primary dispersal from the meltout of a~~
426 ~~localised moraine deposit.~~

427 ~~The medial moraine on Haut Glacier d'Arolla emerged during glacial recession in the second half~~
428 ~~of the 20th century (Reid et al., 2012), offering an example of a recently developed debris cover.~~
429 ~~The debris covered part of Suldenerferner developed its continuous debris cover since the~~
430 ~~beginning of the 19th century, when the glacier was mapped with debris cover below ~2500 m~~
431 ~~and only surficial medial moraine bands extending up to 2700 m (Finsterwalder and Lagally,~~
432 ~~1913). The Nepalese glaciers are thought to have been debris covered for longer (Rowan,~~
433 ~~2016), although it remains unclear when their debris covers first developed.~~

434 The percentage frequency distributions shown in Fig. 5, viewed in the context of the relative
435 'maturity' of the debris covers sampled, are suggestive of a progressive change in skewness and
436 kurtosis of debris thickness variability over time, as debris accumulates at the surface and
437 undergoes progressively more gravitational reworking and/or the underlying ice tongue
438 stagnates. The more mature debris covers on the Ngozumpa and Lirung glaciers is generally
439 thick and characterised by hummocky terrain (cf. Fig. 2b), dissected with ponds and ice faces;
440 whereas, the less mature debris cover on Suldenerferner is generally thinner and the terrain is
441 less hummocky, with relief primarily associated with incision by supraglacial streams. Similarly,
442 the observed progressive change in thickness and skewness/kurtosis of the debris sites
443 downglacier on the Ngozumpa glacier would reflect the downglacier increase in maturity of the
444 debris covered surface downglacier, as well as progressive stagnation of the underlying ice.

445 5.2 Ablation modelling using mean and variable debris thickness

446 Ablation was calculated ~~for using the different mean debris thickness and debris thickness~~
447 variability measured at the three locations study areas on the Ngozumpa glacier (Fig. 2a; Fig. 5;
448 Fig. 6a) encompassing different mean debris thickness and debris thickness variability (Fig. 5;
449 Fig. 6a), that might reflect different stages in debris cover maturity (see Section 5.1), but it
450 should be noted that the sampling method and sample number differs between locations (Table
451 2).

452 The ablation calculated for typical August conditions at the pyramid weather station using the
453 mean debris thickness ~~for at the Margin, Gokyo and Uplacier sites~~ was 2.2, 3.6 and 10.5 mm
454 day⁻¹ (Fig. 6c), totalling each location on the glacier totalled 0.07, 0.11 and 0.32-33 m of ice
455 surface lowering over the month ~~at the 1, 2 and 7 km sites~~ respectively. This agrees with the
456 general expected patterns of ablation gradient reversal towards the terminus of a debris-
457 covered glacier (e.g. Benn and Lehmkuhl, 2000; Bolch et al., 2008; Benn et al., 2017). Accounting
458 for the percentage frequency distribution of debris thickness at the Margin, Gokyo and
459 Uplacier sites increased the surface lowering rate to 2.5, 5.2 and 15.0 mm day⁻¹, giving monthly
460 total surface lowering ~~due to ablation to of~~ 0.08, 0.16 and 0.46 m, ~~at 1, 3 and 7 km,~~ respectively.
461 In these illustrative examples, using a mean debris thickness instead of the local frequency
462 distribution of debris thickness, underestimates the ablation rate at these sites in these cases by
463 11-30 % over a month of ~~typical-representative~~ August conditions (Fig. 6c). These values are
464 specific to the cases presented here but can be considered indicative of the order of ~~of~~ the effect
465 of using mean debris thickness instead of the local variable debris thickness. Considering the
466 maximum and minimum error bounds of the debris thickness distribution (Fig. 6a and c)
467 ~~increases-expands~~ the range of this underestimate to 10-40%. This suggests that ~~-~~ while
468 modelled ablation using local mean debris thickness can provide a lower bound- ~~this~~ and ~~also~~
469 other measures of central tendency (~~tested but not shown here~~), are likely to be poor ~~metrics~~
470 inputs for ablation modelling for typical debris cover. Instead, sufficient data points of debris
471 thickness to capture the local variability are likely to give a more reliable ablation estimate from
472 model simulations. As the melt rate in the 'thin debris' part of the Østrem curve responds more
473 sensitively to changes in debris thickness than it does in the 'thick debris' part of the curve, the
474 impact of accounting for local spatial variability in debris thickness varies inversely with debris
475 thickness (Fig. 6c). This is compounded by the fact that thinner debris appears to have more
476 skewness and kurtosis in the percentage frequency distribution of debris thickness, meaning
477 that the offset between the calculated mean debris thickness and the typical debris thickness is
478 likely to be greater. Coupled with the previous interpretations of how the skewness of debris
479 thickness distribution relates to the relative maturity of the debris cover, this implies that the
480 difference between sub-debris ablation calculated with a mean debris thickness of the thickness
481 distribution will be greatest for recently developed or emerging debris cover.

482 Highly variable debris thickness can be expected to impact methods of mapping debris
483 thickness using thermal-band satellite imagery, as our data show that the debris thickness
484 variability within individual pixels of a thermal-band satellite image may be large. The modelled
485 surface temperature for mean August conditions was 19.5, 19.0 and 16.6°C for the mean debris
486 thickness at the Mmargin, Gokyo and Uuplacier study areas respectively. Accounting for the
487 local debris variability at the lowest-Margin site altered the calculated surface temperature by
488 < 0.1°C, and, at the middle-Gokyo and upper-Uplacier ~~locationssites~~, reduced the calculated
489 surface temperatures by 0.5 and 1.5°C respectively (Fig. 6d). This highlights the manner in
490 which variable debris thickness can be expected to influence the pixel values in satellite thermal
491 imagery, whereby a mean debris thickness calculated from a pixel temperature can be expected
492 to underestimate the true mean debris thickness.

493 5.3 Relationships between debris thickness and terrain properties

494 | Visual inspection of the radargrams indicates that the thickest debris is found filling
495 | depressions in the underlying ice surface, and thinner debris is more commonly seen overlying
496 | steeper ice surfaces ~~thinnest debris cover occurs on steep slopes~~ (Fig. 7a and b). On the basis
497 | that slope failure typically redistributes mass from areas of high slope angle, and that debris
498 | sliding was often experienced while collecting the GPR data, it seems likely that this is the result
499 | of high debris export rates ~~in these from slopes to hollows areas~~ due to frequent or recent slope
500 | failure in the form of sliding events (c.f. Lawson, 1979, Heimsath et al. 2012). ~~Here,~~ On steeper
501 | slopes where the debris surface is approximately parallel to the ice surface, ~~and~~ this appears to
502 | be a characteristic of debris covers at or near the limits of gravitational instability. Localized
503 | areas of thick debris are found below steep slope sections in the form of infilled ice-surface
504 | depressions. Modelled surface flowpaths (Fig. 7b) cross-cut the GPR transects where these
505 | depressions are located, indicating that they were likely incised by meltwater. This suggests
506 | that meltwater is transported in sub-debris supraglacial channels (c.f. Miles et al. 2017), but also
507 | that meltwater routing is a local control on debris thickness by providing topographic lows that
508 | become infilled by debris. Additionally, it seems likely that meltwater channels undercut steep
509 | slopes, thereby causing debris failure. Steep slopes on debris-covered glaciers are relatively
510 | short, so undercutting would have the combined effect of increasing slope angle and also
511 | reducing the confining force (or buttressing effect) imparted by down-slope debris cover. In
512 | some places, thick debris is contained behind pinning points of the underlying ice (Fig. 7a and
513 | b), which results in the occurrence of talus slopes (Fig. 7a), this stabilizes the debris and
514 | increases the confining force. Thick debris on convex, divergent terrain provides evidence of
515 | topographic inversion due to differential ablation (Fig. 7c).

516 | The single glacier ~~M~~margin transect shows increasing debris thickness towards the glacier
517 | margin (Fig. 4b and Fig. 7e). This is expected as a result of: (i) material delivered onto the
518 | glacier from the inner flanks of the lateral moraines as they are progressively debutressed by
519 | glacier surface lowering; and (ii) lower surface velocities at the glacier margins, hence slower
520 | debris advection rates. The Ngozumpa glacier and others in the region typically have troughs at
521 | the boundary between the glacier and the lateral moraine, and evidence of thicker debris here
522 | reinforces the idea that these troughs are eroded by meltwater routed along the glacier margins
523 | (Benn et al., 2017).

524 | Since 1984, the ~~development-existence~~ of supraglacial ponds within the Gokyo study area is
525 | likely to have affected two areas of radar transects: Several transects towards the north of the
526 | Gokyo study area, which ~~were partially~~ may have been partially affected by lakes in 2012 and
527 | 2014, and a single transect towards the east of the Gokyo study area, which crossed clearly
528 | lacustrine surface deposits was partially affected by lakes in all the sampled years except 2014
529 | and 2016 (Fig. 4). One of the transects towards the north of the Gokyo study area shows thick
530 | debris and some internal structures (Fig. 7e) including what may be a relict slump structure,
531 | where a package of sediment fell into the lake from its margin as the lake expanded (e.g. Mertes
532 | et al. 2016). Thick debris in former supraglacial lakes is likely due to high sedimentation rates in
533 | the ponds and by slumping at lake margins during lake expansion (Mertes et al. 2016).
534 | Modelling suggests that subaqueous sub-debris melt rates are low (Miles et al. 2016), so debris
535 | thickening caused by the melt-out of englacial debris is likely to be minimal. The radar
536 | stratigraphy over former lake beds suggests multiple near surface reflectors that can reasonably

537 be interpreted as fine lake sediments overlying coarser supraglacial diamict, suggesting that the
538 locally thicker sediments associated with lakes are due to deposition from sediment-rich
539 supraglacial and englacial meltwaters flowing into a more sluggishly circulating pond.

540 The debris thickness sampled with GPR in this study does not show distinct relations with
541 surface slope, aspect or curvature, that could be readily extracted from glacier surface terrain
542 models (-Fig. 8a, b, c). Binning the thickness data with respect to surface slope indicates a non-
543 statistically significant step decrease in debris thickness above surface slope angles of around
544 20-23° (Fig. 8a). This may represent a transition from the low debris transport rates expected
545 on low-gradient, stable slopes, to the high-debris transport rates expected on steep, failure-
546 prone slopes. While slope and curvature are relatively evenly sampled by the dataset, the same
547 is not true for aspect. While southerly and north-easterly aspects are well sampled, samples are
548 scarce in other aspect sectors, rendering interpretation of potential aspect controls on debris
549 thickness difficult (Fig. 8e). Tentatively, our data suggests thin debris is scarcer for
550 northwesterly aspects, than others (Fig. 8b, e). Comparing the GPR measurements with both
551 slope and aspect simultaneously (Fig. 8e) shows what would be expected from Fig. 8a and 8b:
552 That debris tends to be thicker on northwest facing slopes, and thinner on steeper slopes away
553 from the north-westerly sector. During the pre-monsoon in the Himalaya, more melting is likely
554 to occur on southeast-facing slopes than southwest-facing slopes because clouds often reduce
555 incoming shortwave radiation in the afternoon (e.g. Kurosaki and Kimura, 2002; Bhatt and
556 Nakamura, 2005, Shea et al., 2015). This effect is observable in global radiation data (Fig. 8d).
557 Distributing incoming shortwave radiation on slopes of different slopes and aspects reveals the
558 northwest sector to be the one receiving least solar radiation in midsummer conditions (Fig. 8f).
559 As a result slopes in this sector may be expected to produce less meltwater meaning that debris
560 water content, pore pressure remain low, maintaining higher shear strength and greater
561 stability, allowing thicker debris to be sustained even on steep slopes (Moore, 2017). Samples
562 from steep slopes in the south-east sector are scarce, likely due to the higher melt rates
563 resulting from higher solar radiation receipts, serving to reduce slope angles here (Buri and
564 Pellicotti, 2018). As a result of the absence of steep slopes in the southeast sector, minimum
565 debris thicknesses are displaced to steeper slope angles flanking the aspect sector or highest
566 midsummer solar radiation receipts. No significant correlations were found between surface
567 curvature and debris thickness (Fig. 8c), but perhaps this is to expected, as the GPR samples
568 only a snapshot of a dynamically evolving surface. Depending on the stage of topographic
569 inversion sampled, thicker debris could be found at the hummock summit or in the surrounding
570 troughs. Furthermore, the predominance of slope failure over slope creep mechanisms of
571 gravitational reworking would serve to mask any existing relationship with curvature.
572 Ultimately, it seems that the relationship between debris thickness and morphometric terrain
573 parameters (slope, aspect and curvature) is complex.

574 *5.4 Slope stability modelling*

575 Slope stability modelling suggests that, under mid-August ablation conditions, the percentage of
576 the debris-covered area interpreted as potentially unstable for the three study areas of
577 Ngozumpa Glacier is between 13 and 34% including ponds and ice cliffs, and between ~~12 and~~
578 ~~22%-10 and 32%~~ if ponds and ice cliffs are excluded (Fig. 9). The percentage of potentially
579 unstable surface area increases upglacier, as debris thickness decreases and ablation rates

580 increase (Fig. 6c). Oversteepening was found to be the dominant cause of instability in all three
581 study areas, meaning that the debris is most likely to be unstable where surface slope is greater
582 than $\sim 27^\circ$ (i.e. greater than the inverse tangent of the debris-ice interface friction coefficient). ~~In~~
583 ~~the Gokyo and upglacier study areas,~~ saturation excess was found to be the second most
584 important cause of instability and meltwater weakening the third. ~~Here, it seems that the debris~~
585 ~~is thin enough and ablation rates high enough for the debris to become saturated with surface~~
586 ~~meltwater. In the downglacier margin study area, however, meltwater weakening was found to~~
587 ~~be more important than saturation excess, presumably because the debris here is considerably~~
588 ~~thicker and ablation rates providing meltwater are lower.~~

589 On the basis that thin debris is more likely to exist on unstable slopes, or on slopes that have
590 recently failed, and that debris-covered glaciers typically extend to lower elevations than
591 debris-free glaciers, these results have important implications for debris-covered glacier surface
592 mass balance. Debris gravitational instability provides a mechanism by which relatively large
593 parts of debris-covered glaciers can experience reworking that exposes the underlying glacier
594 ice to high melt rates, even if the debris cover is generally thick.

595 Perturbing slope stability model input variables by 10% generally resulted in small changes of
596 up to 1% in areal percentage slope instability, indicating the model is relatively robust.
597 However, adjusting the debris-ice friction coefficient by 10% caused relatively large changes of
598 up to 9%. Increasing melt rate and the density of water to the density of wet debris ratio cause
599 areal percentage slope instability to increase. Increasing hydraulic conductivity, the debris-ice
600 friction coefficient, and debris thickness cause areal percentage slope instability to decrease. It
601 is interesting to note that the Uplacier study area is most sensitive to input variable
602 perturbation, presumably because debris is thinner and therefore melt rate are greatest in the
603 Uplacier study area.

604 **6. Conclusions**

605 Debris thickness is known to vary over the surfaces of debris-covered glaciers due to advection,
606 rockfall from valley sides, movement by meltwater, and slow cycles of topographic inversion.
607 The debris thickness data presented here suggest that the local debris thickness variability may
608 show characteristic changes in skewness and kurtosis associated with progressive thickening
609 and/or reworking of debris cover over time. On this basis the likely distribution of debris
610 thickness might be predicted by the maturity, or time elapsed since development, of the debris
611 cover found on a glacier surface.

612 For the thickly debris-covered glaciers of the Himalaya, sub-debris melt rates across the
613 ablation zones are generally considered to be small compared to sub-aerial melt rates at ice
614 cliffs (e.g. up to 5 cm d⁻¹, Watson et al. 2016) and sub-aqueous bare ice melt rates at supraglacial
615 lakes (e.g. 2-4 cm d⁻¹, Miles et al. 2016). Our GPR data confirm that the debris cover on
616 Ngozumpa Glacier is typically thick, with the thickest debris found on shallower-gentle slopes, in
617 depressions, or at the sites of former supraglacial ponds. Here, the debris is too thick for the
618 daily temperature wave to penetrate to the ice (Nicholson and Benn, 2012). Consequently, even
619 in core ablation season conditions, typical melt rates are low across most of the debris covered
620 area. However, processes of debris destabilization can form areas of thin debris within the
621 generally thicker debris cover. These areas of thinner debris skew the spatially-averaged

622 ablation rate in a manner that is analogous to that caused by exposed ice faces. Here, sub-debris
623 melt rates under thinner debris are expected to be significantly above average, and even
624 comparable with bare ice melt rates further upglacier. We find that using mean debris thickness
625 values in surface mass balance models is likely to cause melt to be underestimated, and our
626 results confirm previous suggestions that debris thickness is better represented in surface mass
627 balance models as a probability density function (e.g. Nicholson and Benn, 2012; Reid et al.,
628 2012).

629 On the surface of the Ngozumpa glacier, our data suggest that topography is an important
630 additional local control on debris thickness distribution, via slope and hydrological processes,
631 and also that thick sediment deposits at the beds of former supraglacial ponds are an
632 important additional control on the local variability of debris thickness. Surface debris appears
633 to be mobilized and transported by slope- and aspect-dependent sliding caused by sub-debris
634 melting, and most likely triggered by meltwater activity. Debris is redistributed from steep to
635 more gentle slopes ~~to shallow slopes~~ and to ice-surface depressions that are often of
636 hydrological origin. However, the relationship between debris thickness and morphometric
637 terrain parameters is complex. While there is some apparent variation of debris thickness with
638 slope and aspect, whereby thinner debris caused by slope failure is more likely to occur on
639 steeper slopes with aspects that receive more abundant solar radiation, we find no meaningful
640 variation with curvature. This, combined with observations of slide-type debris morphology,
641 suggests that mass movement on the Ngozumpa glacier occurs on relatively short timescales
642 and predominantly by processes that occur at the limits of gravitational stability (e.g. Moore,
643 2017). Slope stability modeling suggests that large areas of the glacier are potentially prone to
644 failure, and thus, as failure forms areas of thinner debris, that melting in these areas might be
645 important at the glacier scale.

646

647 *Data availability* Debris thickness data measured on Ngozumpa glacier ~~will be made publicly~~
648 available on [Zenodo, DOI 10.5281/zenodo.1451559](https://zenodo.org/doi/10.5281/zenodo.1451559).

649 *Author contribution* LN, MM and HP contributed to field data collection. LN analyzed the debris
650 thickness distributions, performed melt modelling and led the preparation of the manuscript.
651 MM, ~~with guidance from HP and IW,~~ processed the GPR data with guidance from HP and IW,
652 performed terrain analysis, and slope stability modelling. All authors contributed to finalizing
653 the manuscript.

654 *Competing interests* The authors declare that they have no conflict of interest.

655 *Acknowledgements* This research is supported by the Austrian Science Fund (FWF) projects
656 V309 and P28521 and the Austrian Space Applications Program of the Austrian Research
657 promotion agency (FFG) project 847999. M.M. is funded by NERC DTP grant number:
658 NE/L002507/1 and receives CASE funding from Reynolds International Ltd. HP was funded by a
659 British Antarctic Survey collaboration grant. The field team in Nepal was U Blumthaler, M
660 Chand, C del Gobbo, A Groos, A Lambrecht, C Mayer, H Pritchard, L Rieg and A Wirbel. C Klug
661 generated the DEM. Debris thicknesses data on Haut Glacier d'Arolla was collected by M
662 Carenzo, F Pellicciotti and L Peterson and provided by T Reid.

663 **References**

- 664 Arthern, R. J., Winebrenner, D. P. and Vaughan, D. G.: Antarctic snow accumulation mapped
665 using polarization of 4.3-cm wavelength microwave emission, *J. Geophys. Res. Atmos.*, 111(6),
666 1–10, doi:10.1029/2004JD005667, 2006.
- 667 Benn, D. I., Wiseman, S. and Hands, K. a.: Growth and drainage of supraglacial lakes on
668 debris-mantled Ngozumpa Glacier, Khumbu Himal, Nepal, *J. Glaciol.*, 47(159), 626–638,
669 doi:10.3189/172756501781831729, 2001.
- 670 Benn, D. I., Wiseman, S. and Warren, C. R.: Rapid growth of a supraglacial lake, Ngozumpa
671 Glacier, Khumbu Himal, Nepal, in *IAHS Publication*, vol. 264, pp. 177–185., 2000.
- 672 Benn, D., Thompson, S., Gulley, J., Mertes, J., Luckman, A. and Nicholson, L.: Structure and
673 evolution of the drainage system of a Himalayan debris-covered glacier, and its relationship
674 with patterns of mass loss, *Cryosphere*, 11(5), 2247–2264, doi:10.5194/tc-11-2247-2017, 2017.
- 675 Benn, D.I., Kirkbride, M., Owen, L.A. and Brazier, V.: Glaciated Valley Landsystems. In: D.J.A.
676 Evans (Ed), *Glacial Landsystems*. Arnold, 2003.
- 677 Bhatt, B. C. and Nakamura, K.: Characteristics of Monsoon Rainfall around the Himalayas
678 Revealed by TRMM Precipitation Radar, *Mon. Weather Rev.*, 133(1), 149–165,
679 doi:10.1175/MWR-2846.1, 2005.
- 680 Bolch, T., Buchroithner, M., Pieczonka, T. and Kunert, A.: Planimetric and volumetric glacier
681 changes in the Khumbu Himal, Nepal, since 1962 using Corona, Landsat TM and ASTER data, *J.*
682 *Glaciol.*, 54(187), 592–600, doi:10.3189/002214308786570782, 2008.
- 683 Buri, P., Pellicciotti, F., Steiner, J. F., Evan, S. and Immerzeel, W. W.: A grid-based model of
684 backwasting of supraglacial ice cliffs on debris-covered glaciers, *Ann. Glaciol.*, 57(71), in press,
685 doi:10.3189/2016AoG71A059, 2016.
- 686 Buri, P. and Pellicciotti, F.: Aspect controls the survival of ice cliffs on debris-covered glaciers,
687 *Proc. Natl. Acad. Sci.*, in revisio(Xx), 1–23, doi:10.1073/pnas.1713892115, 2018.
- 688 [del Gobbo, C.: Debris thickness investigation of Solda glacier, southern Rhaetian Alps, Italy:
689 Methodological considerations about the use of ground penetrating radar over a debris-covered
690 glacier. MSc Thesis, University of Innsbruck, 2017](#)
- 691
- 692 Conway, H. and Rasmussen, L. A.: Summer temperature profiles within supraglacial debris on
693 Khumbu Glacier, Nepal, in *IAHS Publication*, vol. 264, pp. 89–97, 2000.
- 694 Evatt, G. W., Abrahams, I. D., Heil, M., Mayer, C., Kingslake, J., Mitchell, S. L., Fowler, A. C. and
695 Clark, C. D.: Glacial melt under a porous debris layer, *J. Glaciol.*, 61(229), 825–836,
696 doi:10.3189/2015JoG14J235, 2015.
- 697 Fawcett, T.: An introduction to ROC analysis, *Pattern Recognit. Lett.*, 27(8), 861–874,
698 doi:10.1016/j.patrec.2005.10.010, 2006.

- 699 Finsterwalder, S. and Jagally, M.: Die Neuvermessung des Suldenferers 1906 und dessen
700 Veränderungen in den letzten Jahrzehnten. *Zeitschrift für Gletscherkunde*, 13, 1-7, 1913.
- 701 Foster, L. a., Brock, B. W., Cutler, M. E. J. and Diotri, F.: A physically based method for estimating
702 supraglacial debris thickness from thermal band remote-sensing data, *J. Glaciol.*, 58(210), 677-
703 691, doi:10.3189/2012JG11J194, 2012.
- 704 Gibson, M. J., Glasser, N. F., Quincey, D. J., Mayer, C., Rowan, A. V. and Irvine-Fynn, T. D. L.:
705 Temporal variations in supraglacial debris distribution on Baltoro Glacier, Karakoram between
706 2001 and 2012, *Geomorphology*, 295, 572-585, doi:10.1016/j.geomorph.2017.08.012, 2017.
- 707 Heimsath, A. M., Dietrichs, W. E., Nishiizumi, K. and Finkel, R. C.: The soil production function
708 and landscape equilibrium, *Nature*, 388(6640), 358-361, doi:10.1038/41056, 1997.
- 709 Herreid, S. and Pellicciotti, F.: Automated detection of ice cliffs within supraglacial debris cover,
710 *Cryosph. Discuss.*, (October), 1-33, doi:10.5194/tc-2017-205, 2017.
- 711 Hirschmüller, H.: Stereo processing by semiglobal matching and mutual information. *IEEE*
712 *Transaction on Pattern Analysis and Machine Intelligence*, 30 (2), 328-341, 2008.
- 713 | Hock, R. & Noetzli, C.: Area melt and discharge modelling of Storglaciären, Sweden, *Ann.*
714 *Glaciol.*, 24, 211-216, doi:10.1017/S0260305500012192, 1997
- 715 Ishikawa, M., Watanabe, T. and Nakamura, N.: Genetic differences of rock glaciers and the
716 discontinuous mountain permafrost zone in Kanchanjunga Himal, Eastern Nepal, *Permafr.*
717 *Periglac. Process.*, 12(3), 243-253, doi:10.1002/ppp.394, 2001.
- 718 Juen, M., Mayer, C., Lambrecht, A., Han, H. D. and Liu, S.: Impact of varying debris cover thickness
719 on ablation: a case study for Koxkar Glacier in the Tien Shan, *Cryosph.*, 8(2), 377-386,
720 doi:10.5194/tc-8-377-2014, 2014.
- 721 Kayastha, R. B., Takeuchi, Y., Nakawo, M. and Ageta, Y.: Practical prediction of ice melting
722 beneath various thickness of debris cover on Khumbu Glacier, Nepal, using a positive degree-
723 day factor, in *IAHS Publication*, vol. 264, pp. 71-81., 2000.
- 724 Kirkbride, M. P.: Ice-marginal geomorphology and Holocene expansion of debris-covered
725 Tasman Glacier, New Zealand, *IAHS Publ.*, (264), 211-217, 2000.
- 726 Kraaijenbrink, P. D. A., Bierkens, M. F. P., Lutz, A. F. and Immerzeel, W. W.: Impact of a global
727 temperature rise of 1.5 degrees Celsius on Asia's glaciers, *Nature*, 549(7671), 257-260,
728 doi:10.1038/nature23878, 2017.
- 729 Kurosaki, Y. and Kimura, F.: Relationship between Topography and Daytime Cloud Activity
730 around Tibetan Plateau., *J. Meteorol. Soc. Japan*, 80(6), 1339-1355, doi:10.2151/jmsj.80.1339,
731 2002.
- 732 Loomis, S.R.: Morphology and ablation processes on glacier ice. *Proceedings of the Association*
733 *of American Geographers*, 12: 88-92, 1970.

734 Mattson, L.E., Gardner, J.S. and Young, G.J.: Ablation on debris covered glaciers: an example from
735 the Rakhiot Glacier, Punjab, Himalaya. In: G.J. Young (Ed.), Snow and glacier hydrology. IAHS-
736 IASH Publication 218, Wallingford, pp. 289-296, 1993

737 McCarthy, M., Pritchard, H. D., Willis, I. and King, E.: Ground-penetrating radar measurements of
738 debris thickness on Lirung Glacier, Nepal, *J. Glaciol.*, 63(239), 534–555,
739 doi:10.1017/jog.2017.18, 2017.

740 Mertes, J. R., Thompson, S. S., Booth, A. D., Gulley, J. D. and Benn, D. I.: A conceptual model of
741 supra-glacial lake formation on debris-covered glaciers based on GPR facies analysis, *Earth Surf.*
742 *Process. Landforms*, 42(6), 903–914, doi:10.1002/esp.4068, 2017.

743 Mihalcea, C., Brock, B. W., Diolaiuti, G., D’Agata, C., Citterio, M., Kirkbride, M. P., Cutler, M. E. J. and
744 Smiraglia, C.: Using ASTER satellite and ground-based surface temperature measurements to
745 derive supraglacial debris cover and thickness patterns on Miage Glacier (Mont Blanc Massif,
746 Italy), *Cold Reg. Sci. Technol.*, 52(3), 341–354, 2008.

747 Mihalcea, C., Mayer, C. and Diolaiuti, G.: Spatial distribution of debris thickness and melting from
748 remote-sensing and meteorological data, at debris-covered Baltoro glacier, Karakoram,
749 Pakistan, *Ann. Glaciol.*, 48, 49–57, 2008.

750 Mihalcea, C., Mayer, C., Diolaiuti, G., Lambrecht, A., Smiraglia, C. and Tartari, G.: Ice ablation and
751 meteorological conditions on the debris-covered area of Baltoro glacier, Karakoram, Pakistan,
752 *Ann. Glaciol.*, 43(1894), 292–300, 2006.

753 Miles, E. S., Pellicciotti, F., Willis, I. C., Steiner, J. F., Buri, P. and Arnold, N. S.: Refined energy-
754 balance modelling of a supraglacial pond, Langtang Khola, Nepal, *Ann. Glaciol.*, 57(71), 29–40,
755 doi:10.3189/2016AoG71A421, 2016.

756 Miles, K. E., Hubbard, B., Irvine-Fynn, T. D. L., Miles, E. S., Quincey, D. J. and Rowan, A. V.: Review
757 article: The hydrology of debris-covered glaciers; state of the science and future research
758 directions, *Cryosph. Discuss.*, 1–48, doi:10.5194/tc-2017-210, 2017.

759 Montgomery, D. R. and Dietrich, W. E.: A physically based model for the topographical control on
760 shallow landsliding, *Water Resour. Res.*, 30(4), 1153–1171, doi:10.1029/93WR02979, 1994.

761 Moore, P. L.: Stability of supraglacial debris, *Earth Surf. Process. Landforms*,
762 doi:10.1002/esp.4244, 2017.

763 Nicholson, L. I. and Benn, D. I.: Calculating ice melt beneath a debris layer using meteorological
764 data, *J. Glaciol.*, 52(178), 463–470, 2006.

765 Nicholson, L. I. and Benn, D. I.: Properties of natural supraglacial debris in relation to modelling
766 sub-debris ice ablation, *Earth Surf. Process. Landforms*, 38(5), 409–501, doi:10.1002/esp.3299,
767 2012.

768 Nicholson, L. I. and Mertes, J. R.: Thickness estimation of supraglacial debris above ice cliff
769 exposures using a high-resolution digital surface model derived from terrestrial photography, *J.*
770 *Glaciol.*, 1–10, doi:10.1017/jog.2017.68, 2017

- 771 | Nuimura, T., Fujita, K., Yamaguchi, S. and Sharma, R. R.: Elevation changes of glaciers revealed
772 | by multitemporal digital elevation models calibrated by GPS survey in the Khumbu region,
773 | Nepal Himalaya, 1992–2008, *J. Glaciol.*, 58(210), 648–656, doi:10.3189/2012JoG11J061, 2012
- 774 | Østrem, G.: Ice melting under a thin layer of moraine, and the existence of ice cores in moraine
775 | ridges. *Geografiska Annaler*, 51(4): 228-230, 1959.
- 776 | Pelletier, J. D. and Rasmussen, C.: Geomorphically based predictive mapping of soil thickness in
777 | upland watersheds, *Water Resour. Res.*, 45(9), doi:10.1029/2008WR007319, 2009.
- 778 | Quincey, D. J., Luckman, A. and Benn, D. I.: Quantification of Everest region glacier velocities
779 | between 1992 and 2002, using satellite radar interferometry and feature tracking, *J. Glaciol.*,
780 | 55(192), 596–606, doi:10.3189/002214309789470987, 2009.
- 781 | Reid, T. D. and Brock, B. W.: Assessing ice-cliff backwasting and its contribution to total ablation
782 | of debris-covered Miage glacier, Mont Blanc massif, Italy, *J. Glaciol.*, 60(219), 3–13,
783 | doi:10.3189/2014JoG13J045, 2014.
- 784 | Reid, T. D. and Brock, B. W.: An energy-balance model for debris-covered glaciers including heat
785 | conduction through the debris layer, *J. Glaciol.*, 56(199), 903–916, 2010.
- 786 | Reid, T. D., Carenzo, M., Pellicciotti, F. and Brock, B. W.: Including debris cover effects in a
787 | distributed model of glacier ablation, *J. Geophys. Res.*, 117(D18), 1–15,
788 | doi:10.1029/2012JD017795, 2012.
- 789 | [Rieg L., Klug C., Nicholson L., Sailer R. : Pléiades tri-stereo data for glacier investigations –](#)
790 | [Examples from the European Alps and the Khumbu-Himal, *Remote Sens.*, 10\(10\), 1563; doi:](#)
791 | [10.3390/rs10101563, 2018](#)
- 792 | Rounce, D. R. and McKinney, D. C.: Debris thickness of glaciers in the Everest Area (Nepal
793 | Himalaya) derived from satellite imagery using a nonlinear energy balance model, *Cryosph.*,
794 | 8(1), 1317–1329, doi:10.5194/tc-8-1317-2014, 2014.
- 795 | Sakai, A., Takeuchi, N., Fujita, K. and Nakawo, M.: Role of supraglacial ponds in the ablation
796 | process of a debris-covered glacier in the Nepal Himalayas, in *IAHS Publication*, vol. 265, pp.
797 | 119–132, 2000.
- 798 | Schauwecker, S., Rohrer, M., Huggel, C., Kulkarni, A., Ramanathan, A. L., Salzmann, N., Stoffel, M.
799 | and Brock, B. W.: Remotely sensed debris thickness mapping of Bara Shigri Glacier, Indian
800 | Himalaya, *J. Glaciol.*, 61(228), 675–688, doi:10.3189/2015JoG14J102, 2015.
- 801 | Shea, J. M., Wagnon, P., Immerzeel, W. W., Biron, R., Brun, F. and Pellicciotti, F.: A comparative
802 | high-altitude meteorological analysis from three catchments in the Nepalese Himalaya, *Int. J.*
803 | *Water Resour. Dev.*, (May), 1–27, doi:10.1080/07900627.2015.1020417, 2015.
- 804 | Thompson, S. S., Benn, D. I., Dennis, K. and Luckman, A.: A rapidly growing moraine-dammed
805 | glacial lake on Ngozumpa Glacier, Nepal, *Geomorphology*, 145–146, 1–11,
806 | doi:10.1016/j.geomorph.2011.08.015, 2012.

- 807 Thompson, S. S., Benn, D. I., Mertes, J. and Luckman, A.: Stagnation and mass loss on a Himalayan
808 debris-covered glacier: Processes, patterns and rates, *J. Glaciol.*, 62(233), 467–485,
809 doi:10.1017/jog.2016.37, 2016.
- 810 Wagnon, P., Vincent, C., Arnaud, Y., Berthier, E., Vuillermoz, E., Gruber, S., Ménégoz, M., Gilbert,
811 A., Dumont, M., Shea, J. M., Stumm, D. and Pokhrel, B. K.: Seasonal and annual mass balances of
812 Mera and Pokalde glaciers (Nepal Himalaya) since 2007, *Cryosphere*, 7(6), 1769–1786,
813 doi:10.5194/tc-7-1769-2013, 2013.
- 814 | [Washburn, B.: Mapping Mount Everest, *Bull. Am. Acad. Arts Sci.*, 42\(7\), 29–44, 1989.](#)
- 815 | Watson, C. S., Quincey, D. J., Carrivick, J. L. and Smith, M. W. ~~M. W. M. W. M. W. M. W.~~: The
816 dynamics of supraglacial ponds in the Everest region, central Himalaya, *Glob. Planet. Change*,
817 142, 14–27, doi:10.1016/j.gloplacha.2016.04.008, 2016.
- 818 Zhang, Y., Fujita, K., Liu, S., Liu, Q. and Nuimura, T.: Distribution of debris thickness and its effect
819 on ice melt at Hailuoguo glacier, southeastern Tibetan Plateau, using in situ surveys and ASTER
820 imagery, *J. Glaciol.*, 57(206), 1147–1157, doi:10.3189/002214311798843331, 2011.
- 821 |

822 *Table 1: Details of processing steps applied to radargrams, in order of use from left to right, using*
 823 *REFLEXW software. T is the period of the transmitted signal, t is two-way travel time and f is*
 824 *operating frequency.*

operating frequency (MHz)	plateau declip	DC shift	dewow (ns)	align first breaks	timezero correct (s)	back-ground removal	band-pass filter	gain
200	whole profile	whole profile	1.5T (7.5)	whole profile	7.6719e-10	whole profile	0.25f, 0.5f, 1.5f, 3f	divergence compensation (scaling 0.1t)
600			1.5T (7.5)		3.2022e-10			

825

Table 2: Statistics of sampled debris thickness variability measured at different locations on Ngozumpa, and other, glaciers by a range of methods.

glacier	method	source	n	m	sample/m	mean	mode	skewness	kurtosis	25%	75%	min	max
Ngozumpa	GPR*	this study (Margin)	13983	238	58.75	3.33	2.19	0.48	1.84	2.23	4.35	1.74	5.96
Ngozumpa	theodolite	Nicholson and Benn, 2012 (Uplacier)	92	460	0.20	1.65	1.87	0.87	3.76	1.05	2.14	0.12	4.36
Ngozumpa	GPR*	this study (Gokyo)	130926	3301	39.66	1.95	1.33	1.06	3.60	0.93	2.71	0.18	7.34
Ngozumpa	SIM-MYS	Nicholson and Mertes, 2017	1011	980	1.00	1.82	0.75	1.33	4.13	0.73	2.46	0.02	7.62
Ngozumpa	theodolite*	Nicholson and Benn, 2012 (Downglacier)	143	715	0.20	0.59	0.09	1.93	8.27	0.25	0.92	0.09	3.22
Lirung	GPR points	McCarthy and others, 2017	6198	354	17.51	0.66	0.39	1.07	3.24	0.32	0.93	0.11	2.30
Suldenferner	GPR	del Gobbo, 2017	61136	1000	61.14	0.32	0.29	0.07	3.39	0.26	0.38	0.00	0.74
Suldenferner	excavation	del Gobbo, 2017	101	10100	0.01	0.14	0.10	2.05	7.49	0.06	0.16	0.00	0.67
Arolla	excavation	Reid and others, 2012 [‡]	488	976	0.50	0.07	0.01	6.29	68.86	0.02	0.08	0.01	1.50

* data used in ablation modelling

‡ data from medial moraine only, excluding patchy debris sites (< 0.01m thickness)

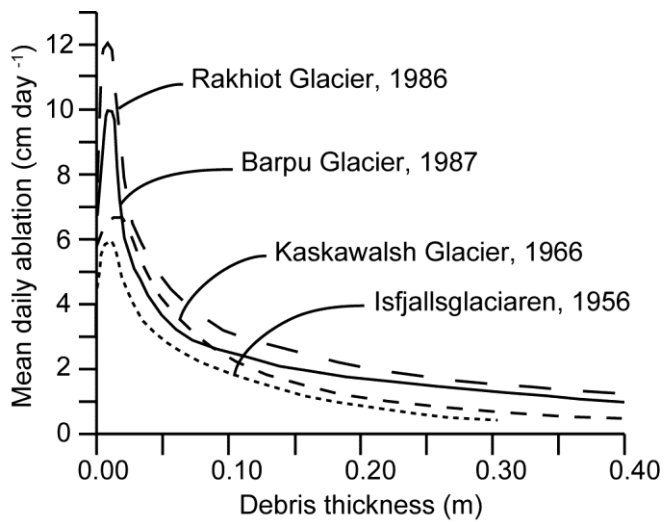


Figure 1: Examples of the relationships between supraglacial debris thickness and underlying ice ablation rate at different glacier sites, redrawn from Mattson et al. (1993). The exact form of this relationship at each site varies with prevailing meteorological conditions and debris properties, but its general character is preserved.

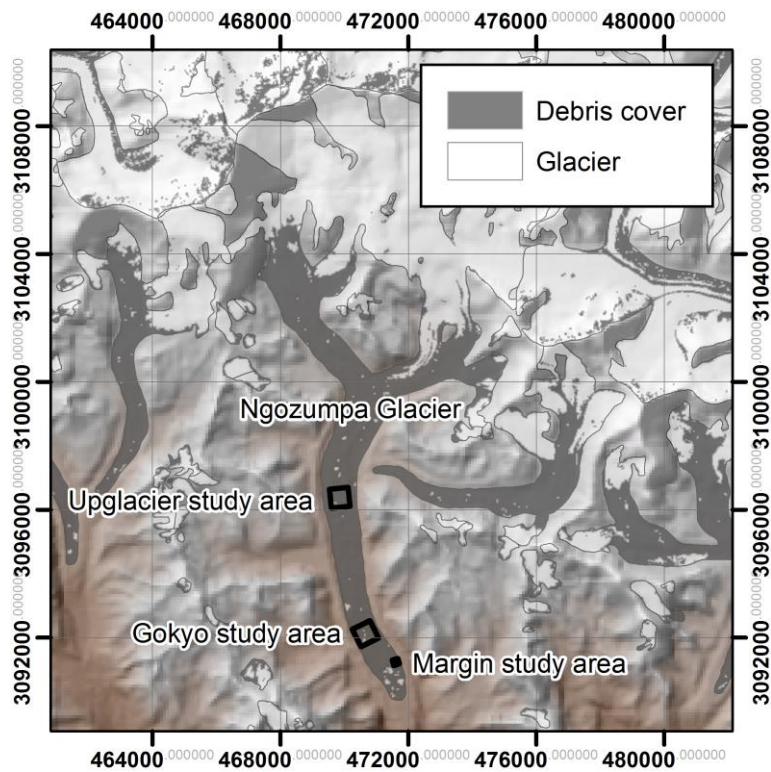


Figure 2: (a) Ngozumpa glacier showing the key study areas, ~7, 2 and 1 km from the glacier terminus at elevations of 4870, 4750 and 4740 m a.s.l. respectively (b) Photograph showing example hummocky terrain in the upglacier study area – note the people for scale in the bottom right corner. Photo credit H. Pritchard.

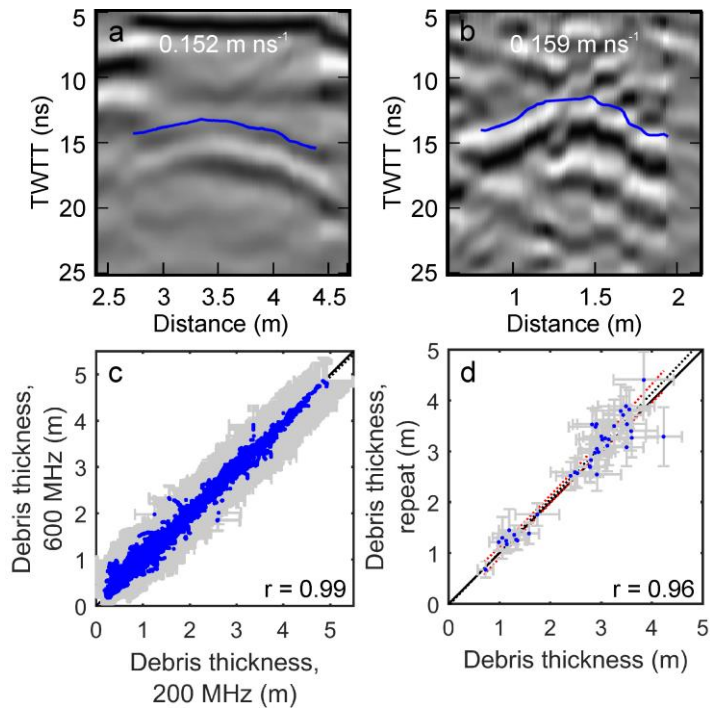


Figure 3: Reflector used to identify signal velocity on Ngozumpa glacier in (a) fine-grained sediments and (b) coarse-grained sediments. Comparison of picked debris ice interface depths sampled simultaneously with different frequencies (c) and at transect intersection points (d).

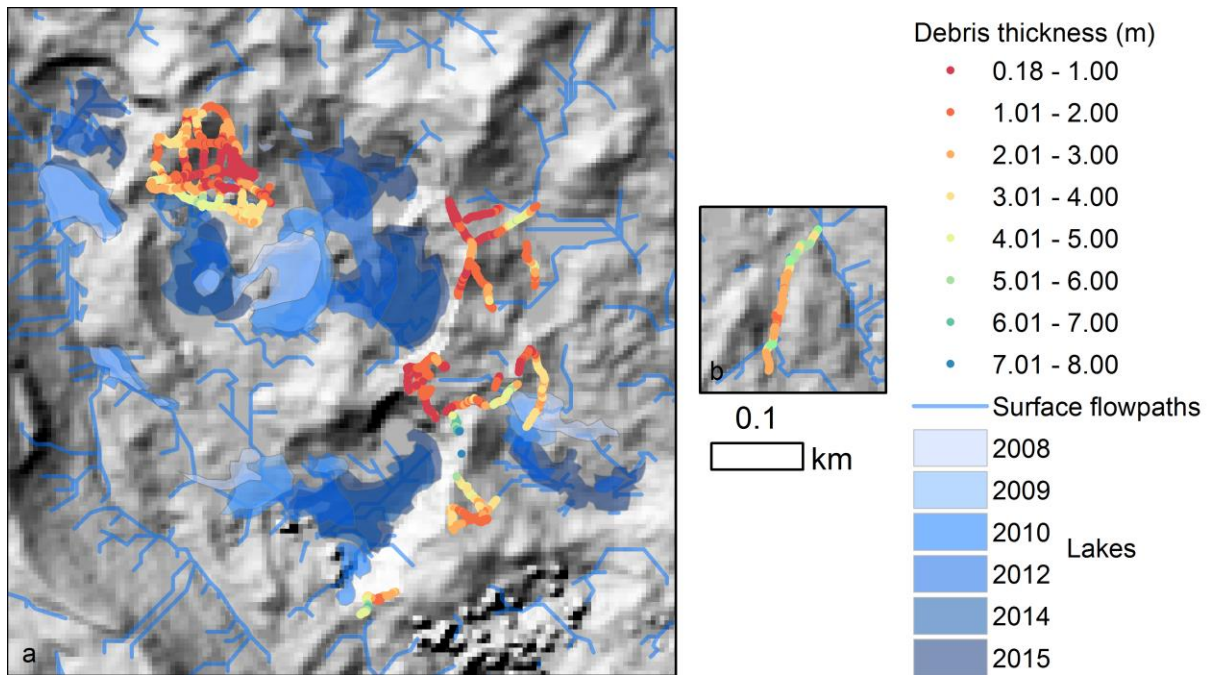


Figure 4: Overview map of GPR debris thickness sampled on Ngozumpa glacier in 2016 overlain on the hillshade from the Pleiades DTM, recent surface pond evolution, and surface flow paths for the Gokyo (a) and Margin (b) study areas (Fig. 2a).

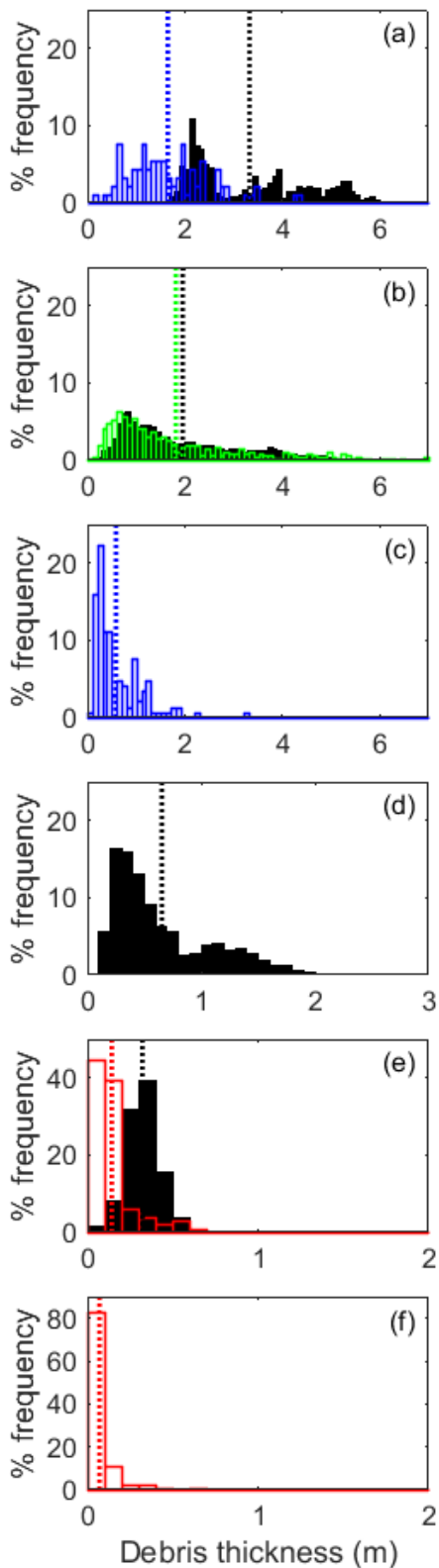


Figure 5: Percentage frequency histograms of debris thickness (h_d) in 0.1 m intervals, and mean debris thickness as vertical dashed lines for (a) the Ngozumpa Margin study site; (b) the Ngozumpa Gokyo study site; (c) the Ngozumpa Upglacier study site; (d) over the lower tongue of Lirung glacier in central Nepal; (e) across the debris covered ablation area of Sulfenerferner/Ghiacciaio de Solda in the Italian Alps and (f) the medial moraine of Haut Glacier

d’Arolla in the Swiss Alps. Measurement methods are GPR (black); theodolite surveys (blue); Structure from Motion (SfM-MVS) photographic terrain model (green) and excavation of pits (red). Note that axes vary between sites, and summary statistics of these distributions are in Table 2.

Figure 5: Percentage frequency histograms of debris thickness (h_d) in 0.05 m intervals at (a) the lower Ngozumpa about 1 km from the terminus; (b) Gokyo area of Ngozumpa, about 2 km from the terminus; (c) upper Ngozumpa, about 7 km from the terminus; (d) over the lower tongue of Lirung glacier in central Nepal; (e) across the debris covered ablation area of Suldenerferner/Ghiacciaio de Solda in the Italian Alps; (f) the medial moraine of Haut Glacier d’Arolla in the Swiss Alps. Measurement methods are GPR (black); theodolite surveys (blue); Structure from Motion (SfM-MVS) photographic terrain model (green) and excavation of pits (red). Note that axes vary between sites, and summary statistics of these distributions are in Table 2.

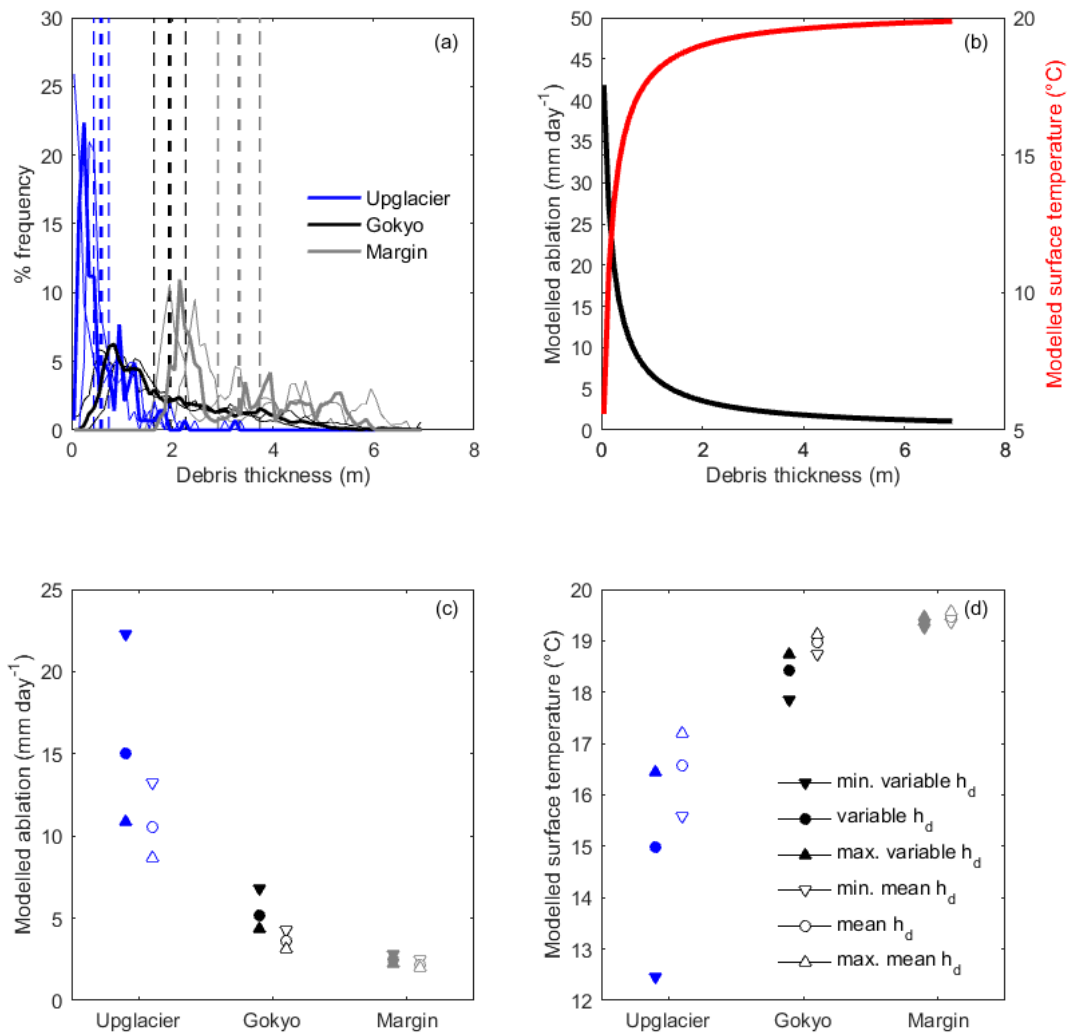


Figure 6: (a) Percentage frequency distributions from the three locations-study sites on Ngozumpa glacier (see Fig. 1). Dashed vertical lines show the \bar{r} , showing the mean debris thickness at each site in dotted vertical lines: 3.33, 1.95 and 0.59 m thick respectively at 1, 2 and 7 km from the terminus. Thinner lines show the values for the maximum and minimum debris thickness conditions calculated from the limits of the individual debris thickness errors. (b) Modelled δ strem curve and surface temperature for mean August conditions. (c) Comparison of modelled ablation for different representations of the debris thickness at each site. (d) Comparison of modelled surface temperature for different representations of the debris thickness at each site.

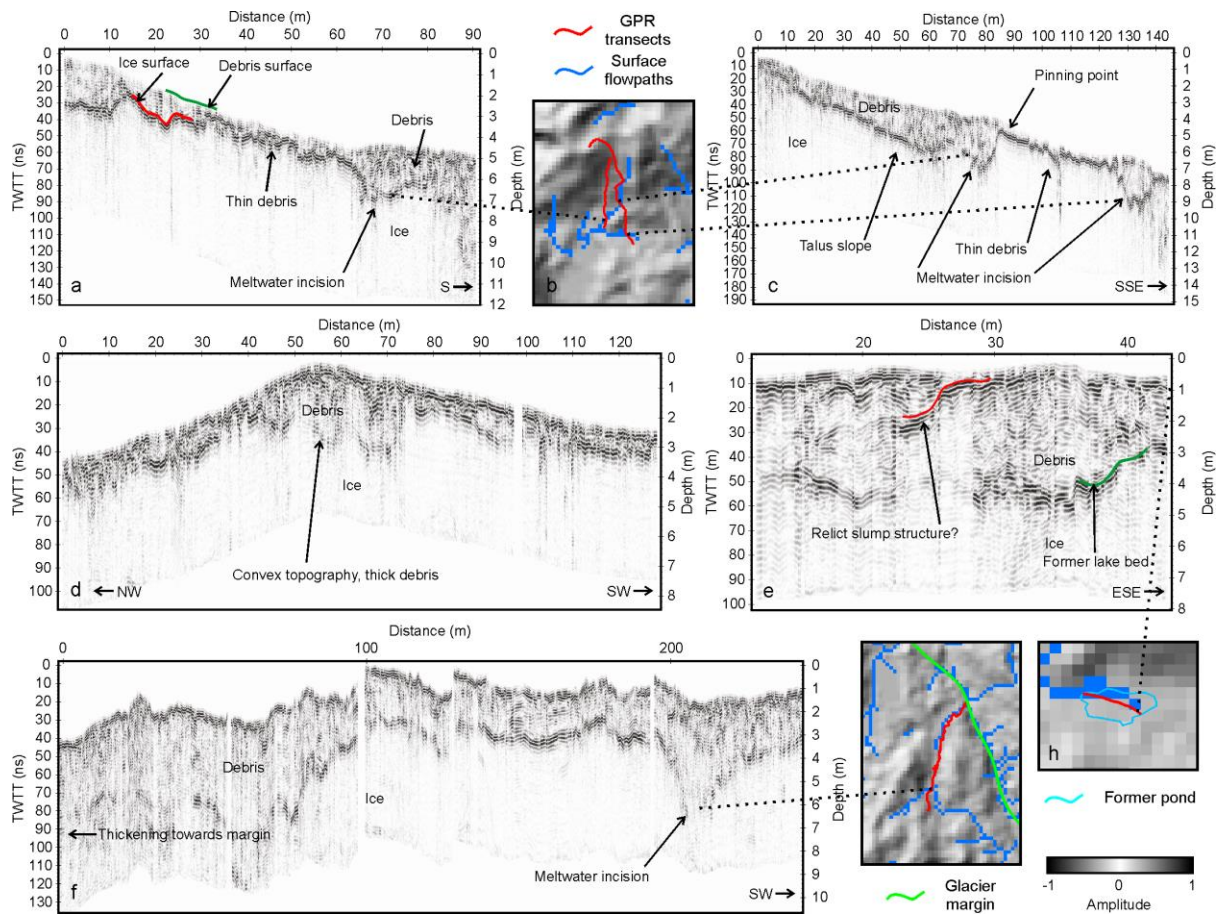


Figure 7: Example radargrams showing debris thickness variability and internal structures in relation to local topography and surface meltwater flow pathways.

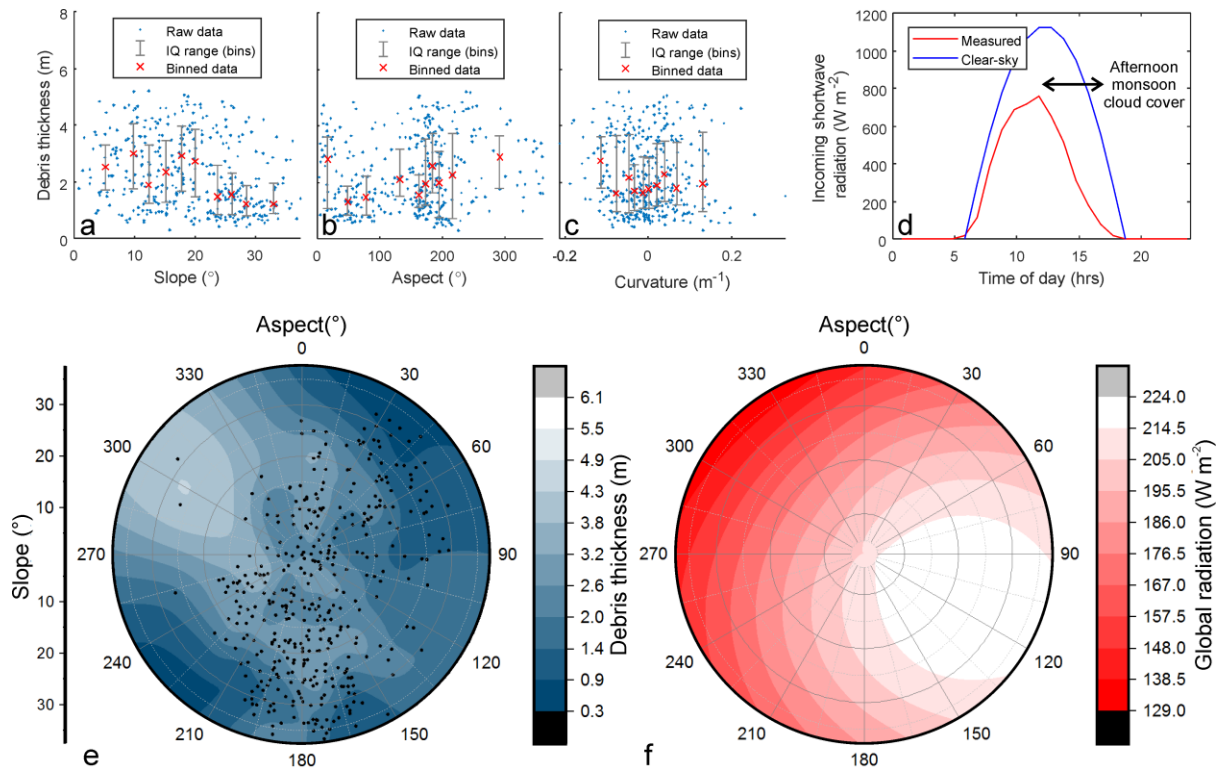


Figure 8: Summary of relationships between measured debris thickness and terrain properties: (a) debris thickness related to local slope angle; (b) debris thickness related to local slope aspect; (c) debris thickness related to curvature (d) August global radiation data collected on the glacier during the survey period; (e) hemispheric plot of debris thickness (showing sub-sampled data points) related to slope angle and aspect; (f) hemisphere plot of August global radiation, distributed on surfaces of different slope and aspect following Hock and Noezli (1997).

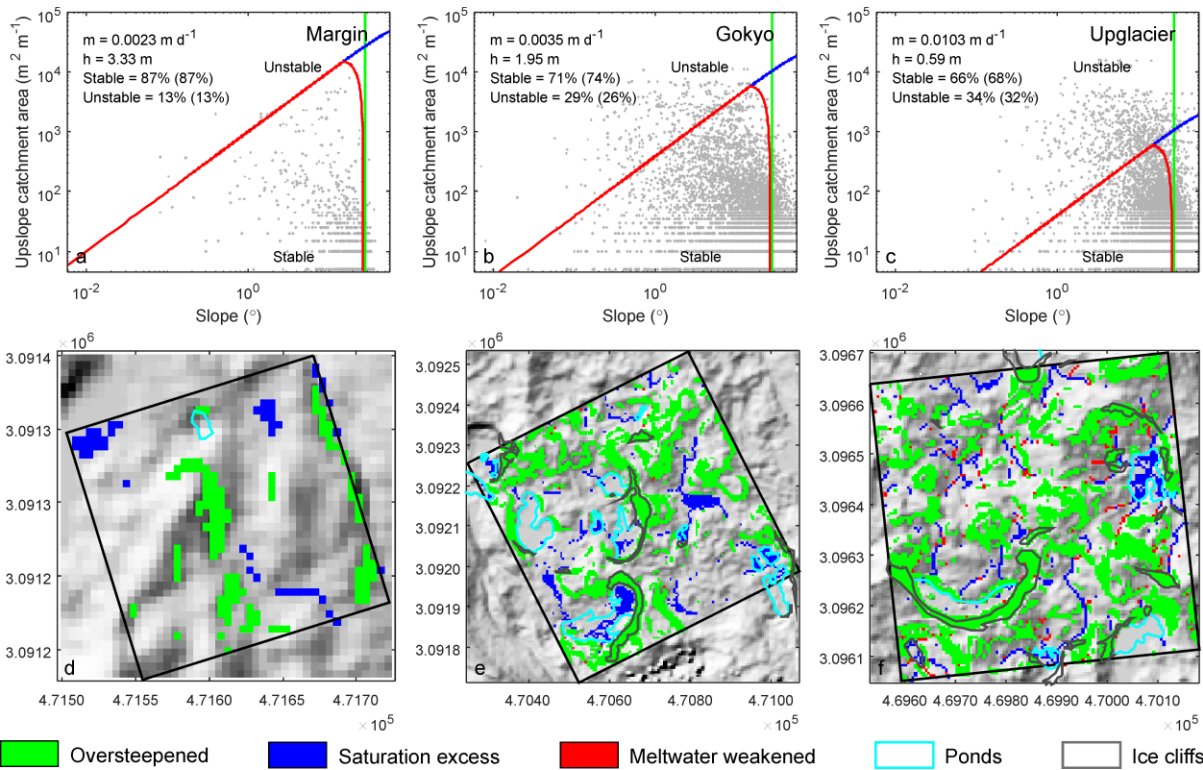


Figure 9: Results of debris stability modelling: Upslope catchment area as a function of slope angle for the three study areas (a-c); points falling above or to the right of the plotted lines are unstable. Percentage area stability/instability values are given with lakes and ice cliffs included, and in brackets with lakes and ice cliffs excluded. Maps of spatial distribution of terrain stability classifications for each study area (d-f), highlighting ponds and ice cliffs.